



Enhancing Thermoelectric Properties of p-type Mg₃Sb₂-based Zintl Phase Compound by Pb Substitution in the Anionic Framework

Journal:	<i>RSC Advances</i>
Manuscript ID:	RA-ART-05-2014-004889.R2
Article Type:	Paper
Date Submitted by the Author:	17-Jul-2014
Complete List of Authors:	Bhardwaj, Aman; CSIR-Network of Institutes for Solar Energy, Materials Physics & Engineering Division, CSIR-National Physical Laboratory,, MISRA, DINESH; CSIR-Network of Institutes for Solar Energy, Materials Physics & Engineering Division, CSIR-National Physical Laboratory,,

1 **Enhancing Thermoelectric Properties of p-type Mg_3Sb_2 - based Zintl Phase**
2 **Compound by Pb Substitution in the Anionic Framework**

3 A. Bhardwaj¹ and D. K. Misra^{1*}

4 CSIR-Network of Institutes for Solar Energy, Materials Physics & Engineering Division,
5 CSIR-National Physical Laboratory, Dr K.S. Krishnan Marg, New Delhi-110012.

6

7 **Abstract**

8 Mg_3Sb_2 -based Zintl compounds have recently attracted as a potential candidate for
9 thermoelectric application due to their low thermal conductivity and promising thermoelectric
10 performance (i.e. $ZT = 0.6$ at 773 K in $\text{Mg}_3\text{Sb}_{2-x}\text{Bi}_x$). We have reported previously that
11 isoelectronic Bi^{3-} substitution on Sb^{3-} leads to moderate increase in the electrical conductivity,
12 enhanced Seebeck coefficient and reduced thermal conductivity. Herein, we report large
13 enhancement of the electrical conductivity while maintaining the Seebeck coefficient by
14 substituting Pb^{4-} on Sb^{3-} site in $\text{Mg}_3\text{Sb}_{2-x}\text{Pb}_x$ ($0 \leq x \leq 0.3$) alloys. Transport measurement
15 reveals that optimum doping of 10 at% Pb^{4-} on Sb^{3-} enhances the ZT to 0.84 at 773 K which
16 is comparable to bismuth tellurides and selenides industrial materials which are toxic and
17 expensive. The enhancement in ZT is attributed to decrease in lattice thermal conductivity
18 and simultaneously increase in the power factor resulted due to significant increase in the
19 electrical conductivity. We observe that Pb^{4-} substitutions on Sb^{3-} site in $\text{Mg}_3\text{Sb}_{2-x}\text{Pb}_x$ ($0 \leq x \leq$
20 0.3) increases the hole carrier concentration. Electronic transports data of $\text{Mg}_3\text{Sb}_{2-x}\text{Pb}_x$ ($0 \leq x$
21 ≤ 0.3) alloys have been analyzed using a single parabolic band model and have been
22 compared to Mg_3Sb_2 . The relatively high figure of merit and affordable material ingredients

1 coupled with one step synthesis process makes these materials a promising cost effective
2 solution as thermoelectric material.

3 *Corresponding author. E-mail address: misradk@nplindia.org, dakkmisra@gmail.com
4 (DKM)

5

6 1. INTRODUCTION

7 In recent years there has been tremendous amount of effort to identify high
8 performance thermoelectric materials based on inexpensive and relatively abundant
9 constituents for application in power generation and refrigeration in various electronic
10 devices.^{1,2} Many applications of thermoelectric devices can be envisioned. However, their
11 widespread implementation is restricted because of poor performance of thermoelectric
12 materials. Thermoelectric materials performance is primarily determined by a dimensionless
13 quantity, so called thermoelectric figure of merit, $ZT = \frac{\alpha^2 \sigma}{\kappa} T$, where α represents the Seebeck
14 coefficient, σ is the electrical conductivity, T is the absolute temperature and κ (i.e. $\kappa = \kappa_{el} +$
15 $\kappa_{lattice}$) is the thermal conductivity accounting both the electrical (κ_{el}) and lattice (κ_l)
16 contributions.³

17 Thus high ZT materials require to possess large α , high σ and low κ which is rather difficult
18 to optimize all the parameters simultaneously in the bulk conventional crystalline materials.
19 However, several reports show that a partial decoupling between these parameters can be
20 achieved by adapting several strategies namely 1) doping mechanism⁴⁻⁷ 2)
21 nanostructuring/nanocomposite⁸⁻¹² and 3) ideally engineered materials¹³⁻¹⁷ with the electronic
22 properties of a crystal and low thermal conductivity of a glass, so called phonon glass
23 electron crystal (PGEC). Following these concepts, in the last decade, many materials such
24 as Bi_2Te_3 ^{12,18-21}, $\text{AgPb}_m\text{SbTe}_{2+m}$ (LAST)¹⁴, TeAgGeSb ¹⁵, PbTe ^{16,22}, SiGe ^{17,23} and Zintl phase

1 compound^{5,7,24-38} have been widely investigated with their high ZT. Among several class of
2 compounds, Zintl phase is an unique class of materials that possess the structural
3 characteristics needed for phonon–glass electron–crystal properties (PGEC)³⁹ leading to high
4 thermoelectric figure of merit (ZT).^{40,41} They combine distinct regions of covalent bonding
5 ideal for electron–crystal properties and ionically bonded cations that can be easily
6 substituted for precise tuning of electronic properties. This leads to the desired “electron
7 crystal” behavior.^{40,42} The complex structures and disorder creates phonon–glass properties
8 resulting in low lattice thermal conductivity, making many Zintl compounds natural “phonon
9 glasses”.^{43,44} As a consequences of these behaviors, a varieties of Zintl phase compounds
10 such as $\text{Yb}_{14}\text{MnSb}_{11}$,²⁴ Zn_4Sb_3 ,²⁵ $\text{Yb}_9\text{Mn}_{4.2}\text{Sb}_9$,²⁶ filled skutterudites,^{27,28} clathrates,^{29,30}
11 YbZn_2Sb_2 ,³¹ YbCd_2Sb_2 ,³² BaZn_2Sb_2 ,³³ BaGa_2Sb_2 ,³⁴ $\text{Eu}_5\text{In}_2\text{Sb}_6$,³⁵ $\text{Yb}_5\text{In}_2\text{Sb}_6$,³⁶ EuZn_2Sb_2 ,³⁷
12 AZn_2Sb_2 ³⁸ etc. with high ZT materials compared to other state-of-the-art thermoelectric
13 materials have been explored. However, the use of expensive rare earth elements and toxic in
14 majority of Zintl phase materials limits their use in large scale industrial application for
15 power generation and refrigeration.

16 Among several Zintl phase compounds, Mg_3Sb_2 based materials involve a rare-earth
17 free, non-toxic, cheap and abundant constituent which makes them economic and
18 environmentally friendly utilization in power generation. Moreover, these compounds have
19 been recognized as a potential candidate for lithium battery⁴⁵, photoconduction⁴⁶, hydrogen
20 transmitting⁴⁷ and structural applications.⁴⁸ A Zintl phase compound of Mg_3Sb_2 crystallizes
21 both in cubic bixbyite as well as in hexagonal structures.⁴⁹ The cubic bixbyite structure is α -
22 phase of La_2O_3 –type which is the high temperature phase, structured with 80 atoms unit cell
23 with 48 Mg and 32 Sb atoms. At low temperature, below ~ 1200 K, Mg_3Sb_2 crystallizes to
24 Mn_2O_3 type β -phase with unit cell composed of 5 atoms (3 Mg and 2 Sb). The β -phase
25 hexagonal structure (Space group $P\bar{3}m1$ No. 164) consists of two inequivalent Mg sites,

1 denoted as Mg(I) and Mg(II) which are ionic and covalent in nature respectively. Thus, the
2 bonding characteristic of Mg_3Sb_2 is in between metallic and ionic.^{50,51} Similar to the structure
3 of CaAl_2Si_2 structure, the stoichiometric Mg_3Sb_2 compound consists of interspersed $\text{Mg}_2\text{Sb}_2^{2-}$
4 layers (the tetrahedral position in the lattice) and Mg^{2+} cation layers (the octahedral position
5 in the lattice).⁵²

6 The thermoelectric properties of Mg_3Sb_2 have been studied by several groups.⁵³⁻⁵⁶
7 However, due to difficulties in synthesizing hexagonal single phase of Mg_3Sb_2 by using
8 conventional synthesis routes (e.g. ball milling and furnace reaction followed by hot-
9 pressing) presence of measurable content of oxygen at grain boundaries⁵⁶, lack of micro
10 structural details and presence of impurity phases of C and MgC_2 contaminated by graphite
11 die used in hot-pressing⁵⁵ and more importantly inconsistencies in the transport properties
12 (e.g. $ZT \approx 0.55$ at 600 K by Kajikawa et al.⁵⁵ and $ZT \approx 0.21$ at 875 K by Condron et. al.⁵⁶) no
13 significant progress has been made towards its viability for thermoelectric applications.
14 However, recently, Singh et al.⁵⁷ theoretically investigated the detailed electronic structure
15 and transport properties of Zintl phase Mg_3Sb_2 and a series of alloys $(\text{AeMg}_2)\text{Pn}_2$ (Ae= Ca,
16 Sr, Ba; Pn= As, Sb, Bi) compounds in relation to their thermoelectric performance. They
17 claimed that the several promising compositions in this family are not fully optimized in
18 terms of carrier concentration. The differences in electronic structure studied theoretically by
19 them, suggest observing its accessibility by the experiments. Furthermore, several
20 unanswered questions of fundamental nature as noticed from the previous studies,⁵³⁻⁵⁶
21 combined with the relatively high abundance of constituents make this class of materials
22 quite interesting and addresses the detail investigation.

23 Recently, we have studied the thermoelectric properties of single phase p-type Mg_3Sb_2 and
24 its derivative of isoelectronic Bi doped; $\text{Mg}_3\text{Sb}_{2-x}\text{Bi}_x$ ($0 \leq x \leq 0.4$) alloys.⁷ An enhanced $ZT \approx$
25 0.6 at 773K for p- type $\text{Mg}_3\text{Sb}_{1.8}\text{Bi}_{0.2}$ was realized by Bi^{3-} substitution on Sb^{3-} . Unfortunately,

1 despite of high Seebeck coefficient and low thermal conductivity of Mg_3Sb_2 , a moderate
2 value of electrical conductivity was noted.⁷ Herein, we report an enhancement in the
3 electrical conductivity while maintaining the Seebeck coefficient by substituting Pb^{4-} on Sb^{3-}
4 site in $\text{Mg}_3\text{Sb}_{2-x}\text{Pb}_x$ ($0 \leq x \leq 0.3$) alloys. The optimum doping of 10 at% Pb^{4-} on Sb^{3-} enhances
5 the ZT to 0.84 at 773 K which is 40% and >200% larger over the $\text{Mg}_3\text{Sb}_{1.8}\text{Bi}_{0.2}$ ($\text{ZT} \approx 0.6$ at
6 773K)⁷ and parent Mg_3Sb_2 ($\text{ZT} \approx 0.26$ at 773K)⁷ compound respectively. We observe that
7 Pb^{4-} substitutions on Sb^{3-} site in $\text{Mg}_3\text{Sb}_{2-x}\text{Pb}_x$ ($0 \leq x \leq 0.3$) yields a best control of carrier
8 concentration for drastically improving the ZT. The high temperature electronic and thermal
9 transport measurements combined with a single parabolic band model have been used to
10 characterize the thermoelectric properties of $\text{Mg}_3\text{Sb}_{2-x}\text{Pb}_x$ ($0 \leq x \leq 0.3$) alloys.

11 2. EXPERIMENTAL PROCEDURES:

12 Stoichiometric amounts of high purity elements magnesium (Mg; 99.99%, Alfa Aesar),
13 antimony (Sb; 99.99%, Alfa Aesar), and Pb (Pb; 99.99%, Alfa Aesar) for synthesizing
14 $\text{Mg}_3\text{Sb}_{2-x}\text{Pb}_x$ ($0 \leq x \leq 0.3$) samples were blended in mechanical milling and subsequently
15 grounded in an agate mortar. The blended powders were then subjected to spark plasma
16 sintering (SPS) at temperature 1073 K and a pressure of 50 MPa for holding time of 10
17 minutes. The consolidated pellets were 12.7 mm diameter and 2.5 mm thick. The SPS were
18 carried out by evacuating and flashing the SPS chamber with Ar gas several times and finally
19 SPS were performed in high vacuum to avoid the oxidation. SPS eliminates adsorptive gas
20 and impurities existing on the surface of the powder particles which results to very clean
21 samples. The present synthesis strategy employing SPS involves simultaneous melting and
22 consolidation of the stoichiometric $\text{Mg}_3\text{Sb}_{2-x}\text{Pb}_x$ ($0 \leq x \leq 0.3$) at high temperature and
23 pressure following cooling to form relatively very small grains of single $\text{Mg}_3\text{Sb}_{2-x}\text{Pb}_x$
24 composition phase.

1 The gross structural characterization of $\text{Mg}_3\text{Sb}_{2-x}\text{Pb}_x$ ($0 \leq x \leq 0.3$) samples was carried out
2 by powder X-ray diffractometer (Rigaku Mini Flex II) using a graphite monochromator and
3 $\text{CuK}\alpha$ radiation with wavelength $\lambda \approx 1.5406 \text{ \AA}$ along with $\text{CuK}\alpha_2$ filter and rotating anode
4 equipped with powder 2θ diffractometer ranging from 20 to 80 degrees. The microstructure
5 and compositional analysis were investigated by field emission scanning electron microscopy
6 (FE-SEM; Model: SUPRA40 VP, operating at 30 kV) equipped with energy dispersive
7 spectroscopy (EDS) and transmission electron microscopy (TEM, Technai G2 T30; W-Twin)
8 operating at 300 KV. The TEM specimens were prepared in three steps and described
9 elsewhere.⁷

10 The polished SPSeD pellets were used directly for thermal diffusivity measurements
11 parallel to the pressing direction. Specific heat was determined by a DSC instrument (822°
12 Mettler Toledo). The thermal conductivity of the sample was calculated using the relation $\kappa =$
13 $\alpha \times C_p \times \rho$, where κ is the thermal conductivity, α the thermal diffusivity, ρ the
14 geometrical pellet density and C_p the specific heat capacity. The thermal diffusivity, specific
15 heat and density measured for all samples, are presented in supporting information S1, S2 and
16 T1. The polished bars of about $3 \times 2 \times 10 \text{ mm}$ were cut from the consolidated disks and are
17 used to measure the electrical conductivity and Seebeck coefficient in a direction
18 perpendicular to the pressing direction. These bar samples were also used for the thermal
19 conductivity measurement to verify the isotropy of thermal properties.

20

21 **3. RESULTS AND DISCUSSION**

22 **3.1 X- ray Diffraction Analysis:**

23 All the samples were identified for phase purity prior to any transport properties
24 measurement and X-ray diffraction pattern performed on the SPSeD samples are shown in

1 Fig. 2(a) for each composition of $\text{Mg}_3\text{Sb}_{2-x}\text{Pb}_x$ ($0 \leq x \leq 0.3$) alloys. In compositions with $x <$
2 0.30, all the reflections can be indexed to $\beta\text{-Mg}_3\text{Sb}_2$ (JCPDS-00-003-0375) and no secondary
3 phase is observed (Fig. 2a). However, the sample with nominal composition of $\text{Mg}_3\text{Sb}_{1.7}\text{Pb}_{0.3}$,
4 reveals Pb as additional phase together with $\beta\text{-Mg}_3\text{Sb}_2$ which might have precipitated due to
5 its limited solubility in Mg_3Sb_2 . The cell constants were estimated by the POLSQ FORTRAN
6 program⁵⁸ and were found increasing with increasing Pb concentration, being consistent with
7 the Vegard's law as shown in Fig. 2(b). Thus, all the samples of $\text{Mg}_3\text{Sb}_{2-x}\text{Pb}_x$ ($0 \leq x \leq 0.2$)
8 are solid solution phase. It is noteworthy that the increase in the lattice parameters is observed
9 to be consistent with the increasing ionic radii of Pb ions, while the broadening of the peaks
10 is attributed to local strain due to heavier Pb substitution in the Sb sub lattice of Mg_3Sb_2 or
11 due to disorder scattering. No additional peaks other than $\beta\text{-Mg}_3\text{Sb}_2$ peaks in the XRD
12 spectrum of $\text{Mg}_3\text{Sb}_{2-x}\text{Pb}_x$ ($0 \leq x \leq 0.2$) were observed, confirming unambiguously the
13 solubility of Pb in the anionic Sb sub-lattice. A solubility of 10 at% Pb in anionic Sb site in
14 Mg_3Sb_2 observed may be expected similar to other reports.⁵⁹⁻⁶¹

15 3.2 Scanning Electron Microscopy:

16 In order to confirm the phase purity at microscopic scale, homogeneities and compositional
17 analysis of $\beta\text{-Mg}_3\text{Sb}_{2-x}\text{Pb}_x$ ($0 \leq x \leq 0.3$), Field emission-Scanning electron microscopy (FE-
18 SEM) investigation was carried out. The homogeneities of samples $\text{Mg}_3\text{Sb}_{2-x}\text{Pb}_x$ ($0 \leq x \leq 0.2$)
19 were assessed by averaging the compositions at 4 different regions of each sample obtained
20 by Energy dispersive X-ray analysis (EDAX). The average value of composition is shown in
21 table 1 marked as SEM-EDAX compositions. All the samples show macroscopically
22 homogeneous as revealed by SEM-EDAX analysis given in table 1. Fig.3 represents SEM
23 investigation of Mg_3Sb_2 and $\text{Mg}_3\text{Sb}_{1.8}\text{Pb}_{0.2}$ alloys. Morphological evidences as presented in
24 Fig 3(a) and Fig 3(d) for Mg_3Sb_2 and $\text{Mg}_3\text{Sb}_{1.8}\text{Pb}_{0.2}$ respectively show almost similar
25 appearance of microstructures. Energy dispersive spectrum mapping combined with SEM-

1 EDAX was recorded to see qualitatively the presence of any minor impurity other than Mg &
2 Sb and the results are shown in Fig. 3(b). It can clearly be seen that only Mg and Sb, were
3 present in their respective concentrations. Fig 3(c) represent SEM-EADX spectrum of
4 Mg_3Sb_2 sample recorded from a region marked by rectangle (Fig 3a), clearly witnessed the
5 presence of only Mg and Sb. Quantification results estimated from the spectrum (inset Fig
6 3c) clearly reveals the Mg_3Sb_2 composition. Similar investigation such as SEM- imaging,
7 SEM-mapping and SEM - EADX for $\text{Mg}_3\text{Sb}_{1.8}\text{Pb}_{0.2}$ have been presented in Fig. (3d)- (3f)
8 respectively showing homogeneities in terms of composition (see table 1), all the element;
9 Mg, Sb & Pb in their respective concentration as shown in EDAX-mapping (Fig 3e) and
10 SEM-EDAX spectrum and quantification (Fig 3f) with composition very close to the
11 nominal composition of $\text{Mg}_3\text{Sb}_{1.8}\text{Pb}_{0.2}$ alloy.

12 **3.3 Transmission Electron Microscopy Investigation:**

13 The detail microstructures at lattice scale of Mg_3Sb_2 and $\text{Mg}_3\text{Sb}_{1.8}\text{Pb}_{0.2}$ alloys have been
14 carried out by high resolution transmission electron microscopy (HR-TEM). In general
15 bright field electron micrographs obtained from the specimen of Mg_3Sb_2 exhibits a
16 polycrystalline structure throughout the volume of the material (Fig. 4a). A corresponding
17 selected area electron diffraction pattern (SAEDP) as shown in Fig 4(b) reveals a set of
18 Debye rings with fine sharp spots overlapping on individual rings. The analysis of these rings
19 reveals that the material consists of a single phase Mg_3Sb_2 with lattice planes, with lattice
20 planes, h k l: $11\bar{2}0$, $20\bar{2}0$, $11\bar{2}4$, $21\bar{3}\bar{3}$ having inter planer spacing of 0.229, 0.198, 0.142,
21 0.127 nm respectively, of hexagonal crystal structure with lattice parameter $a=4.58$ A, $c =$
22 7.24 A (space group $P\bar{3}m1$). At low magnification (Fig. 4a), the micrograph shows grains
23 with different sizes ranging from 8 nm to 80 nm and significant variation in grey contrast.
24 The elemental composition of Mg_3Sb_2 sample estimated from energy dispersive spectroscopy

1 analysis (EDAX) attached with TEM (Fig 4c) reveals the composition very close to the
2 nominal composition of Mg_3Sb_2 alloy. Several lattice scale images were recorded to
3 understand the presence of different orientations of the crystallographic planes and their
4 interface boundaries at atomic level. Figure 4 (d) presents high resolution transmission
5 electron micrograph (HRTEM) image obtained from sample showing several grains
6 orientated in direction of different planes of Mg_3Sb_2 and several joint interface boundaries.
7 The micrograph (Fig. 4d) clearly reveals that the individual grains are truly crystalline with
8 stacking of different planes and with random orientation with respect to each other. A bright
9 field electron micrograph (Fig.4e) corresponding to the specimen of $\text{Mg}_3\text{Sb}_{1.8}\text{Pb}_{0.2}$ shows a
10 polycrystalline structure similar to Mg_3Sb_2 with relatively smaller grain sizes ranging from 5
11 nm to 60 nm. A corresponding SAEDP (not shown here) confirms $\beta\text{-Mg}_3\text{Sb}_2$ hexagonal
12 structure. The lattice scale images reveals the randomly distributed grains with the inter
13 planer spacing of the planes 112 (0.193 nm), 102 (0.27 nm) and many other planes of Mg_3Sb_2
14 hexagonal crystal structure (Fig. 4f). Interestingly, the lattices associated with grains of
15 $\text{Mg}_3\text{Sb}_{1.8}\text{Pb}_{0.2}$ are observed to be little distorted together with some misfit-type of dislocations
16 at the interfaces as marked by arrows in Fig 4(f). The distortions in the lattices at microscopic
17 level may be originated due to local strain due to substitution of heavy metal Pb at Sb site in
18 the structure of Mg_3Sb_2 .

19 **3.4 Electronic transport properties**

20 To determine the effect of Pb^{4+} substitution on Sb^{3-} site on the thermoelectric properties of
21 $\text{Mg}_3\text{Sb}_{2-x}\text{Pb}_x$, high temperature electrical conductivity, Seebeck coefficient and thermal
22 conductivity were measured. Figure 5(a) displays the temperature dependence of electrical
23 conductivity σ (T), for different doping concentration of Pb in Mg_3Sb_2 alloy. Regardless of
24 the temperature, the electrical conductivity increases with increasing Pb concentration. The σ
25 (T) increases monotonically with temperature for samples upto $x \leq 0.2$ over the entire

1 temperature range of 323 K to 773 K, showing semiconducting behavior. Interestingly, for
2 the case of $\text{Mg}_3\text{Sb}_{1.7}\text{Pb}_{0.3}$, σ (T) decreases with rising temperature up to ~ 673 K showing a
3 metallic behavior and further, above 673 K, it saturates indicating semi-metallic
4 characteristics. Thus increasing Pb concentration in Mg_3Sb_2 leads to a transition from
5 semiconducting to metallic behavior. The room temperature measurements of the Hall
6 coefficient (R_H) were used to determine a Hall carrier concentration ($n_H = 1/R_H e$) for all x-
7 values in $\text{Mg}_3\text{Sb}_{2-x}\text{Pb}_x$ ($0 \leq x \leq 0.3$). As observed in Fig 5(b), carrier concentration increases
8 linearly with x up to $x=0.2$ and further a large increment of n_H for $x=0.3$ was noted. The linear
9 increase in carrier concentration with x upto $x= 0.2$ indicates that the Pb^{4+} is indeed
10 substituting on Sb^{3-} site and a true solid solution exists across series $\text{Mg}_3\text{Sb}_{2-x}\text{Pb}_x$ ($0 \leq x \leq$
11 0.2) which is also confirmed by Vegard's law (Fig1b). The room temperature electrical
12 conductivity, and carrier concentration n_H are used to calculate the room temperature mobility
13 (μ) by a relation $\sigma = ne\mu$ and results are shown in Fig 5(c). It is noted from the graph (Fig
14 4c), that measured Hall mobilities at room temperature are around $11\text{-}13 \text{ cm}^2\text{V}^{-1}\text{s}^{-1}$, and are
15 not changed significantly, leading to the assumption that the carrier concentration primarily
16 dominates the electronic transport.

17 Fig. 5(d-e) represents the temperature dependent Seebeck coefficient and effect of room
18 temperature charge carriers on the Seebeck coefficient of $\text{Mg}_3\text{Sb}_{2-x}\text{Pb}_x$ alloys respectively.
19 The Seebeck coefficients of all the samples are positive, indicating holes as the majority
20 carrier type, consistent with the positive carrier concentration obtained from room
21 temperature Hall measurement as shown in table 1. A decrease in the Seebeck coefficient
22 with increasing carrier concentration (increasing x) is observed (Fig. 5 (e)), following the
23 $n^{-2/3}$ dependence in the equation 1 for a degenerate semiconductor with energy independent
24 scattering. The equation for the $\alpha(T)$ dependence on the carrier concentration can be
25 described in the heavy doping regime as⁶²

$$1 \quad \alpha = \frac{8\pi^2 K_B^2}{3eh^2} m^* T \left(\frac{\pi}{3n} \right)^{\frac{2}{3}} \dots\dots\dots 1)$$

2 Where m^* is the effective mass, T , the temperature and n , the carrier concentration. The
 3 linear dependence of α with temperature is found only at low temperature as is assumed in
 4 this model. The temperature dependent Seebeck coefficient of $Mg_3Sb_{2-x}Pb_x$ (Fig 5d) initially
 5 increases with temperature and attain a peak at 650 K. With further increasing temperature,
 6 beyond 650K, the thermal excitation of electrons in present case begins to reduce the
 7 thermopower (Fig. 5d). We speculate that the thermally excited electrons do not cause a
 8 reduction in the Seebeck coefficient within the measurement range below 650 K. However, a
 9 detail high temperature Hall effect over the entire temperature range should be carried out to
 10 understand the exact mechanism of electronic transport. Thus, we observe that both σ and α
 11 increases with increasing temperature. The electrical conductivity usually depends on both
 12 carrier concentration (n) and mobility (μ). With regard to increase α and σ , we infer that “ n ”
 13 may be decreasing but μ would be increasing with temperature. The simultaneous increase in
 14 sigma and S is not usually expected for semiconductors and would require band structure
 15 information as well as high temperature Hall measurement to have better understanding.

16 The effective mass (m^*) of $Mg_3Sb_{2-x}Pb_x$ ($0 \leq x \leq 0.2$) were calculated from carrier
 17 concentrations (n) using equation 1 and slope of Seebeck coefficient versus temperature plot.
 18 We noticed that effective mass remains almost unchanged across the solid solution of
 19 $Mg_3Sb_{2-x}Pb_x$ ($0 \leq x \leq 0.2$) which is not shown here. Further, assuming only one type of
 20 carrier at lower temperature with the assumption of the acoustic phonon scattering ($\lambda=0$), a
 21 single parabolic model may be expected. The effective mass $m^*= 1.96 m_e$ was used to
 22 calculate the Pisarenko relation at room temperature (Fig 5e). The effective mass $m^*= 1.96$
 23 m_e has been calculated from the experimental Seebeck and Hall carrier concentration for $x=$
 24 0.20 at room temperature using equation 1.

1 As evident from the Pisarenko plot shown in Fig 5(e), the experimental Seebeck coefficient
2 α and n_H fall on or near the curve corresponding to $m^*=1.96 m_e$ for $x=0.2$, suggesting that a
3 single parabolic band may be in good agreeing model for electronic transport of $Mg_3Sb_{2-x}Pb_x$
4 system at low temperatures where only one type of carrier exists. Based on the above analysis
5 at low temperature, one can infer that substitution of Pb doesn't significantly alter the
6 effective mass or mobility of the holes and thereby confirming the electronic transport is
7 mainly monitored by the charge carrier densities.

8 The temperature dependence behavior of power factor of $Mg_3Sb_{2-x}Pb_x$ ($0 \leq x \leq 0.3$) is plotted
9 in Fig 5(f). Regardless of temperature, the power factor increases due to large increase in the
10 electrical conductivity with increasing Pb concentration. However, with increasing
11 temperature, the power factor for all the samples except $x=0.3$ increases with rising
12 temperature and maximized at 673K. The highest power factor is optimized for $Mg_3Sb_{1.8}Pb_{0.2}$
13 at 673K which is 45% larger than the parent Mg_3Sb_2 compound. We believe that Pb^{4-}
14 substitution on Sb^{3-} site yields a best control over electrical conductivity and Seebeck
15 coefficient in order to optimize high power factor.

16 **3.5 Thermal transport properties**

17 Figure 6 shows the temperature dependence of thermal conductivity κ (T) of Mg_3Sb_{2-x}
18 Pb_x alloys. As mentioned in the experimental section that the thermal conductivity are
19 measured in a direction parallel to the pressing direction which is perpendicular to the
20 direction in which the electronic transport is measured. Additionally, the thermal conductivity
21 measurements were performed on the rectangular bar specimens which were used for
22 electrical transport. We find that the variation of about 5% in thermal conductivity, measured
23 in parallel and perpendicular direction. This difference is not significant and lies within the
24 equipment error suggesting near isotropic nature of sample. The isotropic nature could be

1 attributed to the nano-sized powder of Mg_3Sb_2 and $\text{Mg}_3\text{Sb}_{1.8}\text{Pb}_{0.2}$ similar to the behavior in
2 layered structure of Bi_2Te_3 nano-sized powder reported^{12,21,63} where a variations of 5- 10% in
3 κ have been described and attributed to isotropic nature of Bi_2Te_3 sample in nanosized
4 powder sample. Off course micron size powder always exhibit anisotropy which has been
5 reported in layered structure of Bi_2Te_3 material.⁶⁴ Interestingly, the total thermal conductivity
6 decreases with increasing Pb concentration in Mg_3Sb_2 alloy regardless to the temperature as
7 shown in Figure 6(a). Moreover, the total thermal conductivity, κ decreases with increasing
8 temperature indicating $1/T$ type behavior, which is commonly occurred in the bulk crystalline
9 solids. The lowest value of thermal conductivity is 0.23 W/mK for $x = 0.3$ was observed
10 which is attributed to mass fluctuations and grain boundary scattering due to increasing the
11 Pb concentration. We have also verified the variation in thermal conductivity data by
12 measuring the samples with thickness (~ 2.5 mm and 1 mm) to see the effect of heat
13 dissipation on the thermal conductivity. However, only a little variation of 4-5% in κ was
14 observed, which is presented in supporting information S3.

15 The temperature dependence of thermoelectric figure of merit, ZT of $\text{Mg}_3\text{Sb}_{2-x}\text{Pb}_x$
16 alloys is shown in Figure 7. The maximum $ZT \approx 0.84$ at 773 K was optimized for
17 $\text{Mg}_3\text{Sb}_{1.8}\text{Pb}_{0.2}$ which is about $> 200\%$ larger than the ZT value observed in parent Mg_3Sb_2
18 compound and 40 % larger over $\text{Mg}_3\text{Sb}_{1.8}\text{Bi}_{0.2}$ of our previous report. The enhanced ZT is
19 resulted from the significant increase in the electrical conductivity at little expense of
20 Seebeck coefficient with further simultaneous decrease in the total thermal conductivity.

21 4. Conclusions

22 A single solid solution Zintl phase of $\text{Mg}_3\text{Sb}_{2-x}\text{Pb}_x$ ($0 \leq x \leq 0.2$) was ascertained by
23 characterizing the specimens employing XRD, FE-SEM and TEM investigation. Substitution
24 of Pb^{4-} on Sb^{3-} site introduces holes as charge carriers, ascribed by Hall measurement data,

1 and results into large p-type electrical conductivity. It was noted that the Pb substitution
2 yields a best control over thermoelectric properties and does not significantly alter the
3 effective mass or mobility and thereby confining the electronic properties to be mainly
4 monitored by charge carrier densities. Electronic transports data of $\text{Mg}_3\text{Sb}_{2-x}\text{Pb}_x$ ($0 \leq x \leq 0.2$)
5 alloys have been analyzed using a single parabolic band model at low temperature. The peak
6 $ZT \approx 0.84$ at 773 K has been achieved in $\text{Mg}_3\text{Sb}_{1.8}\text{Pb}_{0.2}$ alloy which is about > 200% larger
7 than the ZT value observed in parent Mg_3Sb_2 compound. The enhancement in ZT is due to
8 increase in power factor resulted primarily by large increase in the electrical conductivity and
9 with simultaneous decrease in the thermal conductivity. Additional enhancement in ZT could
10 be expected to increase the power factor and reducing the lattice thermal conductivity by
11 suitable doping. The present ZT value is comparable to with bismuth tellurides and selenides
12 industrial materials which are toxic and expensive. Further, Mg_3Sb_2 -based Zintl compounds
13 being free from expensive rare earth elements, makes these materials cost-effective,
14 environment friendly and abundant for the use of power generation.

15 **Acknowledgement**

16 This work was financially supported by CSIR-TAPSUN (CSIR-NWP-54) programme. The
17 authors thank Prof. R. C. Budhani and Dr. Jiji Pullikotil for useful discussions and comments.
18 We acknowledge Dr. Ajay Dhar (HOD, Metals and Alloys Group) for providing facilities and
19 for his critical comments. Dr. Sunil Pandey (NIMS University, Jaipur) is highly
20 acknowledged for providing the room temperature Hall measurement equipment. One of the
21 authors AB greatly acknowledges UGC-CSIR for financial support. We thank Radheshyam
22 and Naval K. Upadhyay for technical and experimental support.

23 **References**

24 1. B. Raton, *CRC Handbook of Thermoelectrics*, CRC, Florida, USA, 1995.

- 1 2. H. J. Goldsmid, *Thermoelectric Refrigeration*, Temple Press Books Ltd., London, 1964.
- 2 3. G. J. Snyder and E. S. Toberer, *Nat. Mater.*, 2008, **7**, 105.
- 3 4. Y. Pei, A. D. LaLonde, S. Iwanaga and G. J. Snyder, *Energy Environ. Sci.*, 2011, **4**, 2085-
- 4 2089
- 5 5. J. J. Pulikkotil, D. J. Singh, S. Auluck, M. Saravanan, D. K. Misra, A. Dhar and R. C.
- 6 Budhani, *Phys. Rev. B.*, 2012, **86**, 155204.
- 7 6. H. Wang, Y. Pei, A. D. LaLonde and G. J. Snyder, *Adv. Mat.*, 2011, **23**, 1366–1370.
- 8 7. A. Bhardwaj, A. Rajput, A. K. Shukla, J. J. Pulikkotil, A. K. Srivastava, A. Dhar, G.
- 9 Gupta, S. Auluck, D. K. Misra and R. C. Budhani, *RSC Adv.*, 2013, **3**, 8504.
- 10 8. Y. Pei, J. L. Falk, E. S. Toberer, D. L. Medlin and G. J. Snyder, *Adv. Funct. Mater.*, 2011,
- 11 **21**, 241–249.
- 12 9. D. K. Misra, A. Bhardwaj and Sanjay Singh, *J. Mater. Chem. A*, 2014, Advance Article,
- 13 DOI: 10.1039/c4ta01380h
- 14 10. A. Bhardwaj, D. K. Misra, J. J. Pulikkotil, S. Auluck, A. Dhar and R. C. Budhani, *Appl.*
- 15 *Phys. Lett.*, 2012, **101**, 133103.
- 16 11. A. J. Minnich, M. S. Dresselhaus, Z. F. Ren and G. Chen, *Energy Environ. Sci.*, 2009, **2**,
- 17 466.
- 18 12. B. Poudel, Q. Hao, Y. Ma, Y. Lan, A. Minnich, B. Yu, X. Yan, D. Wang, A. Muto, D.
- 19 Vashaee, X. Chen, J. Liu, M. S. Dresselhaus, G. Chen and Z. Ren, *Science*, 2008, **320**,
- 20 634.
- 21 13. Y. Pei, H. Wang and G. J. Snyder, *Adv. Mater.*, 2012, **24**, 6124.
- 22 14. K. F. Hsu, S. Loo, F. Guo, W. Chen, J. S. Dyck, C. Uher, T. Hogan, E. K. Polychroniadis
- 23 and M. G. Kanatzidis, *Science*, 2004, **303**, 818.
- 24 15. J. Androulakis, K. F. Hsu, R. Pcionek, H. Kong, C. Uher, J. J. D'Angelo, A. Downey, T.
- 25 Hogan and M. G. Kanatzidis, *Adv. Mater.*, 2006, **18**, 1170.
- 26 16. K. Ahn, K. Biswas, J. He, I. Chung, V. Dravid and M. G. Kanatzidis, *Energy Environ.*
- 27 *Sci.*, 2013, **6**, 1529.

- 1 17. G. Joshi, H. Lee, Y. Lan, X. Wang, G. Zhu, D. Wang, R. W. Gould, D. C. Cuff, M. Y.
2 Tang, M. S. Dresselhaus, G. Chen and Z. F. Ren, *Nano Lett.*, 2008, **8**, 4670.
- 3 18. S. Yu, J. Yang, Y. Wu, Z. Han, J. Lu, Y. Xie and Y. Qian, *J. Mater. Chem.*, 1998, **8**,
4 1949.
- 5 19. J. Shen, T. Zhu, X. Zhao, S. Zhang, S. Yanga and Z. Yina, *Energy Environ. Sci.*, 2010, **3**,
6 1519.
- 7 20. M. E. Anderson, S. S. N. Bharadwaya and R. E. Schaak, *J. Mater. Chem.*, 2010, **20**,
8 8362.
- 9 21. S. Sumithra, N. J. Takas, D. K. Misra, W. M. Nolting, P. F. P. Poudeu and K. L. Stokes,
10 *Adv. Energy Mater.*, 2011, **1**, 1141.
- 11 22. J. R. Sootsman, H. Kong, C. Uher, J. J. D'Angelo, C. I. Wu, T. P. Hogan, T. Caillat and
12 M. G. Kanatzidis, *Angew. Chem., Int. Ed.*, 2008, **47**, 8618.
- 13 23. R. Basu, S. Bhattacharya, R. Bhatt, M. Roy, S. Ahmad, A. Singh, M. Navaneethan, Y.
14 Hayakawa, D. K. Aswal and S. K. Gupta, *J. Mater. Chem. A*, 2014, **2**, 6922.
- 15 24. S. R. Brown, S. M. Kauzlarich, F. Gascoin and G. J. Snyder, *Chem. Mater.*, 2006, **18**,
16 1873.
- 17 25. G. J. Snyder, M. Christensen, E. Nishibori, T. Caillat and B. B. Iversen, *Nature Mater.*,
18 2004, **3**, 458.
- 19 26. S. K. Bux, A. Zevalkink, O. Janka, D. Uhl, S. Kauzlarich, J. G. Snyder and J. P. Fleurial,
20 *J. Mater. Chem. A*, 2014, **2**, 215.
- 21 27. B. C. Sales, D. Mandrus, R. K. Williams, *Science* 1996, **272**, 1325.
- 22 28. J. W. Graff, X. Zeng, A. M. Dehkordi, J. He and T. M. Tritt, *J. Mater. Chem. A*, 2014,
23 Advance Article.
- 24 29. G. S. Nolas, J. L. Cohn, G. A. Slack and S. B. Schujman, *Appl. Phys. Lett.* 1998, **73**, 178.
- 25 30. H. Kleinke, *Chem. Mater.*, 2010, **22**, 604.

- 1 31. F. Gascoin, S. Ottensmann, D. Stark, S. M. Haile, and G. J. Snyder, *Adv. Funct. Mater.*
2 15, 1860 2005.
- 3 32. X. J. Wang, M. B. Tang, H. H. Chen, X. X. Yang, J. T. Zhao, U. Burkhardt and Y. Grin,
4 *Appl. Phys. Lett.*, 2009, **94**, 092106.
- 5 33. X. J. Wang, M. B. Tang, J. T. Zhao, H. H. Chen, and X. X. Yang, *Appl. Phys. Lett.*, 2007,
6 **90**, 232107.
- 7 34. S. J. Kim and M. G. Kanatzidis, *Inorg. Chem.* 2001, **40**, 3781.
- 8 35. S. M. Park, E. S. Choi, W. Kang, and S. J. Kim, *J. Mater. Chem.* 2002, **12**, 1839.
- 9 36. S. J. Kim, J. R. Ireland, C. R. Kannewurf, and M. G. Kanatzidis, *J. Solid State*
10 *Chem.*, 2000, **155**, 55.
- 11 37. H. Zhang, J. T. Zhao, Y. Grin, X. J. Wang, M. B. Tang, Z. Y. Man, H. H. Chen and X. X.
12 Yang, *J. of chem. Phys.* 2008, **129**, 164713.
- 13 38. G. S. Pomrehn, A. Zevalkink, W. G. Zeier, A. van de Walle and G. J. Snyder, *Angew.*
14 *Chem. Int. Ed.* 2014, **53**, 3422.
- 15 39. G. A. Slack, *In CRC Handbook of Thermoelectrics*, CRC, New York, 1995.
- 16 40. S. M. Kauzlarich, *Chemistry, Structure, and Bonding of Zintl Phases and Ions*, VCH
17 Publishers, New York, 1996.
- 18 41. S. M. Kauzlarich, S. R. Brown and G. J. Snyder, *Dalton Trans.*, 2007, 2099–2107.
- 19 42. A. M. Mills, R. Lam, M. J. Ferguson, L. Deakin and A. Mar, *Coord. Chem. Rev.*, 2002,
20 **233**, 207.
- 21 43. G. A. Slack, *Solid State Physics*, Academic Press, New York, 1979.
- 22 44. E. S. Toberer, A. Zevalkink and G. J. Snyder, *J. Mater. Chem.*, 2011, **21**, 15843.
- 23 45. H. Honda, H. Sakaguchi, I. Tanaka and T. Esaka, *J. Power Sources*, 2003, **123**, 216.
- 24 46. P. Singh and K. K. Sarkar, *Solid State Commun.*, 1985, **55**, 439.
- 25 47. N. Nishimiya, A. Suzuki and S. Ono, *Int. J. Hydrogen Energy*, 1982, **7**, 741.

- 1 48. J. C. Viala, F. Barbeau, F. Bosselet and M. Peronnet, *J. Mater. Sci. Lett.*, 1998, **17**, 757.
- 2 49. M. M. Ripoll, A. Haase and G. Brauer, *Acta Cryst.*, 1974, **B30**, 2006.
- 3 50. J. H. Slowik, *Phys. Rev. B*, 1974, **10**, 416.
- 4 51. L. M. Watson, C. A.W. Marshall and C. P. Cardoso, *J. Phys. F: Met. Phys.* 1984, **14**, 113.
- 5 52. C. Zheng, R. Hoffmann, R. Nesper and H. G. von Schnering, *J. Am. Chem. Soc.*, 1986,
- 6 **108**, 1876.
- 7 53. J. H. Bredt, L. F. Kendall, *Proceedings—IEEE/AIAA* 1966.
- 8 54. D. M. Verbrugge, J. B.J. Van Zytveld, *Non-Cryst. Solids* 1993, **736**, 156.
- 9 55. T. Kajikawa, N. Kimura, T. Yokoyama, *Proceedings of the 22nd International Conference*
- 10 *on Thermoelectrics*, 2003, 305.
- 11 56. C. L. Condrón, S. M. Kauzlarich, F. Gascoin, G. J. Snyder, *J. of Sol. Stat. Chem.*, 2006,
- 12 **179**, 2252.
- 13 57. D. J. Singh and D. Parker *J. of Appl. Phys.* 2013, **114**, 143703.
- 14 58. D. Keazler, D. Cahen, J. Lbers *POLSQ FORTRAN program*, IL: Northwestern University
- 15 Evanston, 1984.
- 16 59. X. Shi, Y. Pei, G. J. Snyder and L. Chen, *Energy Environ. Sci.*, 2011, **4**, 4086.
- 17 60. G. J. Tan, L. W. Liu, C. H. Chi, X. L. Su, S. Y. Wang, Y. G. Yan, X. F. Tang, W. Wong-
- 18 Ng, C. Uher, *Acta Materialia*, 2013, **61**, 7693-7704.
- 19 61. A. F. May, E. F. Larsen and G. J. Snyder, *Physical Rev. B*, 2010, **81**, 125205.
- 20 62. M. Cutler, J. F. Leavy, and R. L. Fitzpatrick, *Phys. Rev.*, 1964, **133**, A1143.
- 21 63. Y. Ma, Q. Hao, B. Poudel, Y. Lan, B. Yu, D. Wang, G. Chen, and Z. F. Ren, *Nano Letter*,
- 22 2008, **8**, 2580-2584.
- 23 64. J. Jiang, L. D. Chen, S. Bai, Q. Yao and Q. Wang, *Scripta Materialia*, 2005,
- 24 **52**, 347–351.
- 25
- 26

1

2 **Figure Caption:**

3 **Figure 1.** Schematic diagram of layered crystal structure of $\text{Mg}_3\text{Sb}_{2-x}\text{Pb}_x$ showing the anionic
4 framework of $[\text{Mg}_2(\text{Sb}/\text{Pb})_2]^{2-}$ with double layer and Mg^{2+} cations between the layers.

5 **Figure 2.** (a) X-ray diffraction (XRD) pattern of $\text{Mg}_3\text{Sb}_{2-x}\text{Pb}_x$ ($0 \leq x \leq 0.3$) alloys. The XRD
6 pattern reveals a single $\beta\text{-Mg}_3\text{Sb}_2$ type Zintl phase solid solution upto $x=0.2$. The Pb peaks
7 were noted for $x=0.3$ together with $\beta\text{-Mg}_3\text{Sb}_2$.

8 **(b)** Plot for Vegard's law following linear trend of cell parameters with increasing Pb
9 concentration showing complete solid solution phase formation of $\text{Mg}_3\text{Sb}_{2-x}\text{Pb}_x$ ($0 \leq x \leq 0.2$)
10 alloys.

11 **Figure 3:** FE-SEM micrographs of (a) Mg_3Sb_2 parent compound showing polycrystalline
12 nature of sample (b) elemental EDAX mapping of Mg_3Sb_2 showing qualitatively the presence
13 of constituent elements Mg and Sb (c) SEM-EDAX of Mg_3Sb_2 confirming the composition,
14 very close to Mg_3Sb_2 as shown in the inset (d) SEM image of $\text{Mg}_3\text{Sb}_{1.8}\text{Bi}_{0.2}$ revealing almost
15 similar type morphology of Mg_3Sb_2 (e) elemental EDAX mapping images, demonstrating the
16 presence of all three constituent elements; Mg, Sn and Pb (f) SEM-EDAX of $\text{Mg}_3\text{Sb}_{1.8}\text{Pb}_{0.2}$
17 showing the same composition as the nominal composition(see inset)

18 **Figure 4.** a) TEM image obtained from the specimen of Mg_3Sb_2 showing highly densified
19 grains b) SAED pattern corresponding to Mg_3Sb_2 , revealing $\beta\text{-Mg}_3\text{Sb}_2$ -type hexagonal
20 structure, c) EDS-TEM patterns recorded from Mg_3Sb_2 confirming its exact composition. d)
21 The lattice scale image of Mg_3Sb_2 exhibiting the presence of different orientations of the
22 crystallographic planes and their interface boundaries. e) Bright field electron micrograph
23 recorded from the specimen of $\text{Mg}_3\text{Sb}_{1.8}\text{Pb}_{0.2}$ showing densely packed grains. f) The lattice

1 scale image of $\text{Mg}_3\text{Sb}_{1.8}\text{Pb}_{0.2}$ demonstrating distorted lattices. HRTEM image shown in the
2 inset (Fig 4f) exhibits misfit type of dislocation at the interfaces marked by arrow.

3 **Figure 5:** a) Temperature dependence of the electrical conductivity of $\text{Mg}_3\text{Sb}_{2-x}\text{Pb}_x$ b) room
4 temperature carrier concentration with increasing x c) room temperature Hall mobility with
5 increasing x d) temperature dependence of the Seebeck coefficient, α (T); (e) Pisarenko plot
6 at 300 K showing the dependence of Seebeck coefficient on the carrier concentration (solid
7 line). The experimental data lie on or near the curve (single parabolic band model) generated
8 for $m^*=1.96$ for $x=0.2$, suggesting all the samples have almost equal effective masses f)
9 temperature dependent power Factor, $(\sigma\alpha^2$ (T)).

10 **Figure 6:** Temperature dependence behaviour of the total thermal conductivity κ (T) and
11 lattice thermal conductivity κ_L of $\text{Mg}_3\text{Sb}_{2-x}\text{Pb}_x$ ($0 \leq x \leq 0.3$).

12 **Figure 7:** Temperature dependence of thermoelectric figure of merit of $\text{Mg}_3\text{Sb}_{2-x}\text{Pb}_x$ ($0 \leq x \leq$
13 0.3)

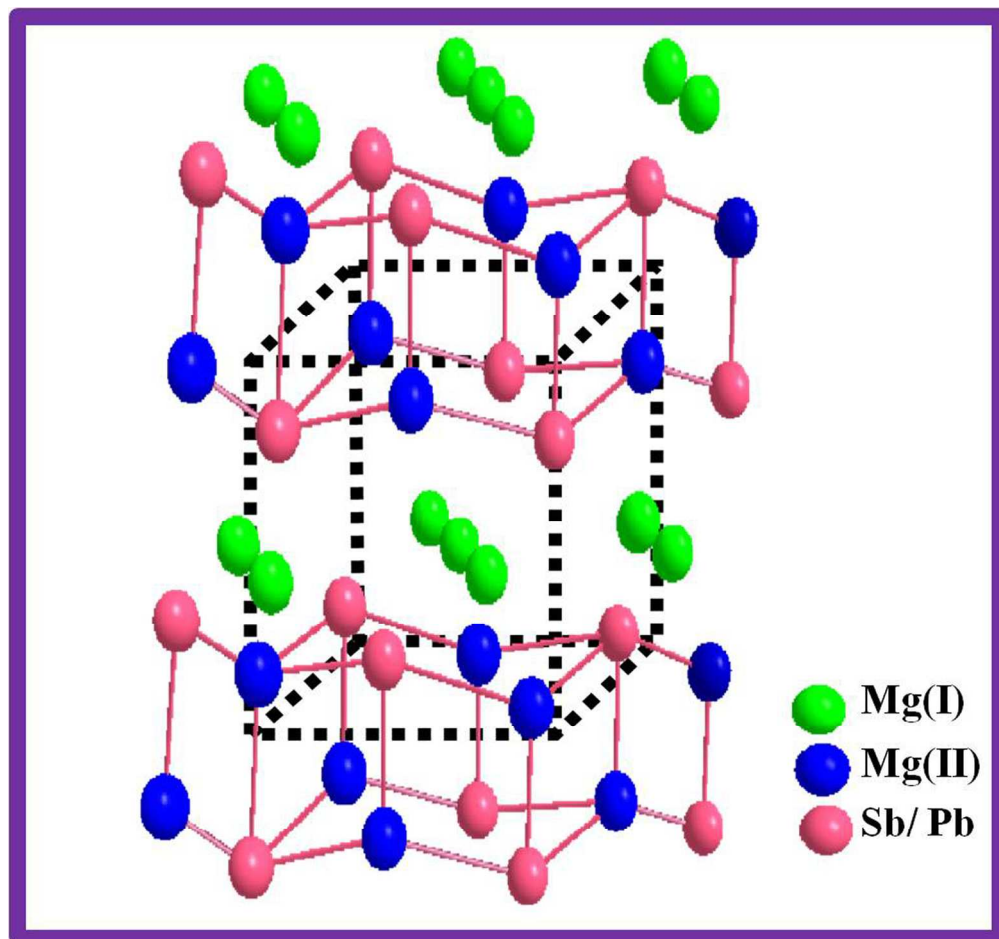
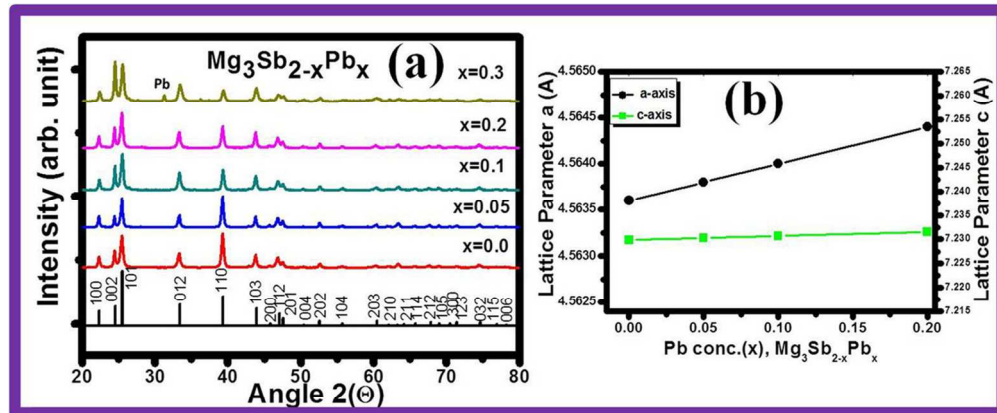


Figure 1

174x179mm (300 x 300 DPI)

**Figure 2**

120x59mm (300 x 300 DPI)

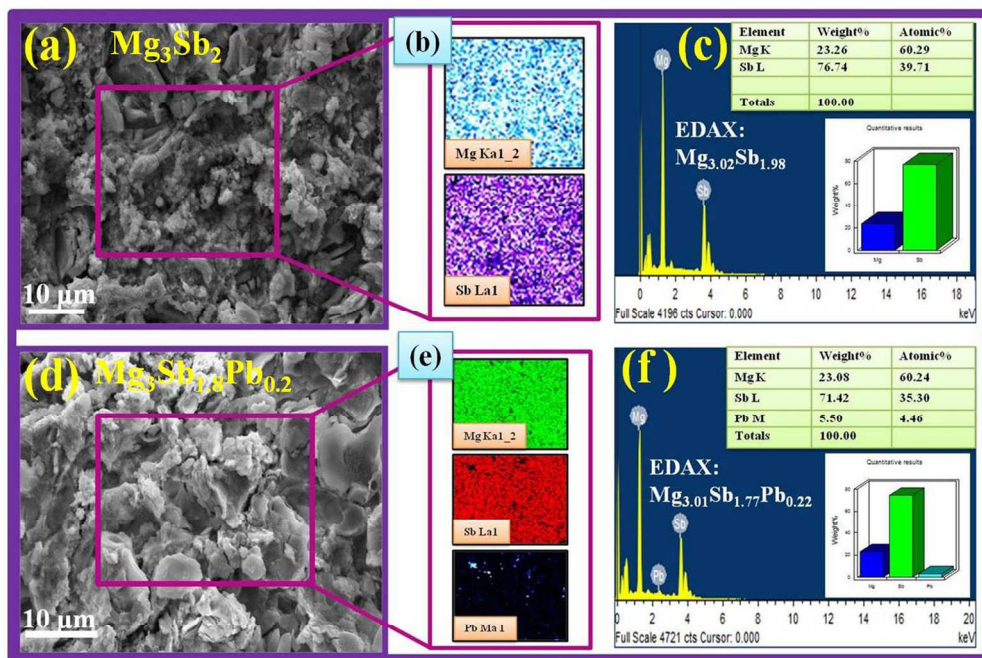


Figure 3

180x132mm (300 x 300 DPI)

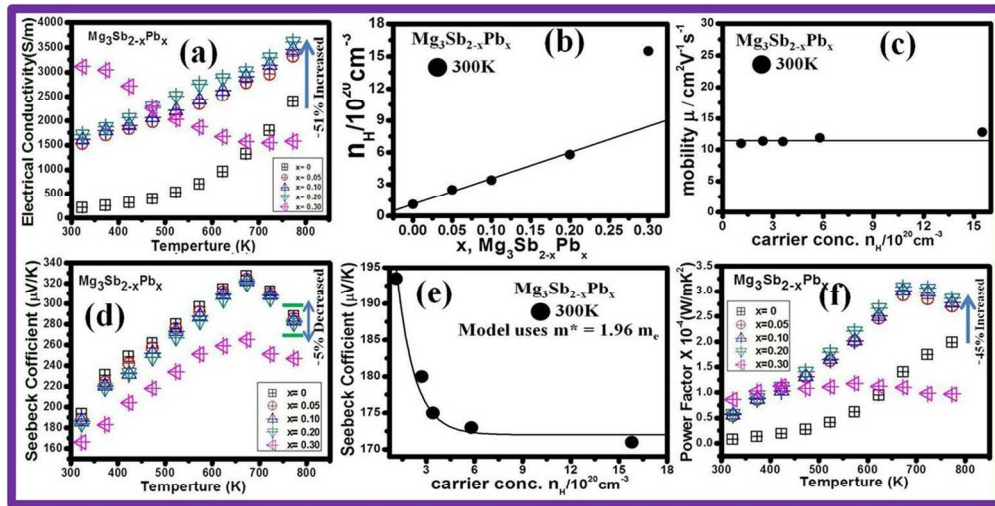


Figure 5

132x76mm (300 x 300 DPI)

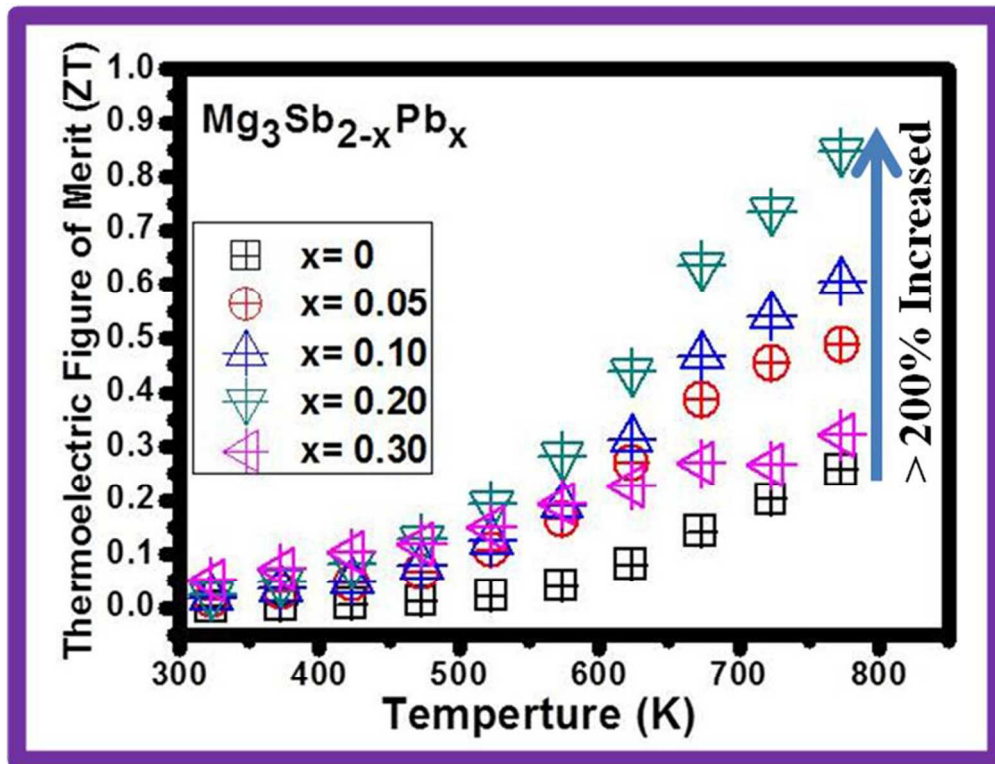


Figure 7

140x121mm (300 x 300 DPI)

Table 1 contains the Hall measurement data and SEM-EDAX composition of $\text{Mg}_3\text{Sb}_{2-x}\text{Pb}_x$ ($0 \leq x \leq 0.3$) alloys.

Nominal Composition	Actual Composition (SEM-EDAX)	Hall Coefficient (R_H) $\times 10^{-2} \text{ cm}^3 \text{ C}^{-1}$	Carrier conc. n (10^{20} cm^{-3})	Mobility μ ($\text{cm}^2 \text{ V}^{-1} \text{ s}^{-1}$)
Mg_3Sb_2	$\text{Mg}_{60.29}\text{Sb}_{39.71}$	5.02	1.2	11
$\text{Mg}_3\text{Sb}_{1.95}\text{Pb}_{0.05}$	$\text{Mg}_{59.82}\text{Sb}_{38.96}\text{Pb}_{1.12}$	2.08	2.9	11.4
$\text{Mg}_3\text{Sb}_{1.90}\text{Pb}_{0.10}$	$\text{Mg}_{59.96}\text{Sb}_{37.98}\text{Pb}_{2.06}$	1.67	3.6	11.7
$\text{Mg}_3\text{Sb}_{1.80}\text{Pb}_{0.20}$	$\text{Mg}_{60.24}\text{Sb}_{35.30}\text{Pb}_{4.46}$	1.04	5.8	12.1
$\text{Mg}_3\text{Sb}_{1.70}\text{Pb}_{0.30}$	$\text{Mg}_{60.34}\text{Sb}_{33.65}\text{Pb}_{6.01}$	0.39	15.5	12.9